TU Delft

Delft University of Technology

Classification of bore patterns induced by storm waves overtopping a dike crest and their impact types on dike mounted vertical walls – A large-scale model study

Streicher, Maximilian; Kortenhaus, Andreas; Marinov, Krasimir; Hirt, Matthias; Hughes, Steven; Hofland, Bas; Scheres, Babette; Schüttrumpf, Holger

DOI
10.1080/21664250.2019.1589635

Publication date
2019

Document Version
Accepted author manuscript

Published in
Coastal Engineering Journal

Citation (APA)
Streicher, M., Kortenhaus, A., Marinov, K., Hirt, M., Hughes, S., Hofland, B., Scheres, B., & Schüttrumpf, H. (2019). Classification of bore patterns induced by storm waves overtopping a dike crest and their impact types on dike mounted vertical walls – A large-scale model study. *Coastal Engineering Journal*, *61*(3), 321-339. https://doi.org/10.1080/21664250.2019.1589635

Important note
To cite this publication, please use the final published version (if applicable).
Please check the document version above.

Copyright
Other than for strictly personal use, it is not permitted to download, forward or distribute the text or part of it, without the consent of the author(s) and/or copyright holder(s), unless the work is under an open content license such as Creative Commons.

Takedown policy
Please contact us and provide details if you believe this document breaches copyrights.
We will remove access to the work immediately and investigate your claim.

This work is downloaded from Delft University of Technology.
For technical reasons the number of authors shown on this cover page is limited to a maximum of 10.

Classification of bore patterns induced by storm waves overtopping a dike crest and their impact types on dike mounted vertical walls – A large-scale model study

Maximilian Streicher[1], Andreas Kortenhaus[1], Krasimir Marinov[2], Matthias Hirt[3], Steven Hughes[4], Bas Hofland[2], Babette Scheres[3], Holger Schüttrumpf [3]

[1] *Dept. of Civil Engineering, Ghent University, Technologiepark 904, B-9052 Zwijnaarde (Ghent), Belgium; email: Maximilian.Streicher@UGent.be*

[2] *Faculty of Civil Engineering and Geosciences, Delft University of Technology, Stevinweg 1, 2628 CN Delft, The Netherlands*

[3] *Institute for Hydraulic Engineering and Water Resources Management (IWW), RWTH Aachen University, Mies-van der-Rohe-Strasse 17, 52056 Aachen, Germany*

[4] *Engineering Research Center, Department of Civil and Environmental Engineering, 1320 Campus Delivery, Colorado State University, Fort Collins, CO 80523-1320, United States*

Classification of bore patterns induced by storm waves overtopping a dike crest and their impact types on dike mounted vertical walls – A large-scale model study

Short duration bores in the coastal zone are generated by wave breaking in shallow water and mild foreshore conditions. In storm weather situations and for sea level rise scenarios these bores approach the dike and interact with previously overtopped or reflected bores. This results in a complex and turbulent interaction process of the water masses before impact on any structure on top of the dike. Combined laser scanner and video measurements were used to study the bore interaction processes. Five bore interaction patterns were distinguished as 1) *regular bore pattern*; 2) *collision bore pattern*; 3) *plunging breaking bore pattern*; 4) *sequential overtopping bore pattern* and 5) *catch-up bore pattern*. Video images of the bore running up the wall and motion tracking of the leading edge were used to obtain a time series of the run-up water at the wall. The impact loads of the bore hitting the wall on the promenade were studied based on the signal of a vertical array of 13 pressure sensors installed over the wall height. Three impact types were distinguished and classified as 1) *impulsive impact type*; 2) *dynamic impact type* and 3) *quasi-static impact type*. The majority of ~2/3 of the total number of impacts were comprised of the *quasi-static impact type*. Links between the bore patterns and impact types were discussed and its implication on force prediction under consideration of possible scale effects highlighted.

Keywords: bore impact; pressure and force; overtopping bore; sea dike; vertical crest wall; large-scale physical model; WALOWA project

INTRODUCTION

There are an increasing number of inhabitants and people visiting the coast, along with growing infrastructure and industry in the coastal zone in Belgium and worldwide. Moreover, according to the assessment of climate change, an increase in sea level and storminess is more likely (IPCC 2014). Hence, the risk in the coastal areas goes up and the demand for a sufficient coastal defense system to protect these areas from flooding and wave impact is apparent. The coasts along Belgium, The Netherlands or Germany are often comprised of shallow waters and a mildly sloping sand foreshore (see Figure 1). At the end of the foreshore a second coastal defense structure may be built, most

often a dike with an attached promenade. The waves transform over the foreshore, and finally a broken wave of short duration approaches and overtops the second coastal defense structure. Overtopped wave impacts are then the result of the interaction between the overtopped wave with any obstacle situated on the promenade. It was previously described that the overtopped wave shows a bore type behavior (Chen et al. 2014). Recently, Lubin & Chanson (2017) proposed to use the analogy of a tidal breaking bore to describe best the similarities to a bore resulting from broken waves. They observed that both bores are highly aerated and tidal bores showed a sequence of splash-ups which are also found in splashing hydrodynamics of breaking waves as well as similarities between bubble plume behavior in tidal bores and breaking waves in the surf zone. Compared to tidal bores, the overtopped bores resulting from an irregular wave field are of very short duration (T=0.5–3s) and prone to interactions with previously overtopped bores, resulting in a complex and turbulent interaction process of the water masses before impact (Table 1). In order to predict reliably the impact loads at the wall, a good understanding of the bore interaction processes is required.

[Figure 1]

Several small-scale experiments were conducted for the above-described situation, using Froude length scale and a scale factor in the range of 1-to-20 until 1-to-35. The impact loads on the structure were investigated for irregular waves (Van Doorslaer et al. 2017; Streicher et al. 2016; Chen 2016; Kortenhaus et al. 2015) and regular waves (Chen et al. 2015). The disadvantage of the small-scale experiments is that generally less air is entrained in the water (Blenkinsopp et al. 2007), which yields in less cushioning effect of the bore impacts and higher measured forces (Bullock et al. 2001). This is expected to lead to an overestimation of the impact loads, when upscaling the results from small-scale to prototype (Cuomo et al. 2010). Prototype tests of overtopped wave loads on a vertical wall were carried out (De Rouck et al. 2012; Ramachandran et al. 2012) in the large wave flume (‘Grosser Wellenkanal’, GWK)

Hannover. In their experimental configuration the influence of the mildly sloping foreshore and shallow waters at the dike toe, that results in broken bores approaching the dike, was not taken into account. Kihara et al. (2015) and Ko et al. (2018) investigated the slightly different situation of long duration (~80s) Tsunami bore impacts on vertical walls. The bore generates a continuous instream of water at the wall and no short duration bore interaction processes prior to impact were observed. A test campaign featuring the overtopping simulator to model the impact of overtopping wave volumes on a storm wall was conducted by Van Doorslaer et al. (2012). A predefined volume of water was released on one side of the promenade and the subsequent impact loads on a wall at the other side of the promenade were measured. In this scenario the interaction between several bores could not be studied, but repeatability between individual tests was improved.

[Table 1]

The first study to distinguish and classify different bore interaction patterns prior to impact was done by Chen (2016) with data derived from small-scale laboratory experiments depicting shallow water and mildly sloping foreshore conditions. She investigated three possibilities of how bore interaction can influence the impact on the wall. For the catch-up pattern (case 1) a first bore is followed by a second and faster bore, they join on the promenade and generate an amplified impact on the wall. The collision pattern (case 2) describes any collision of incoming and reflected bore on the promenade. Depending on the location of the collision this results in an amplified (collision close to wall) or dampened (collision further away from wall) impact. For the wet bed situation (case 3) the incoming bore slides over a residual water layer from a preceding bore. This results in less friction and velocity damping during propagation over the promenade, and subsequently the impact is amplified. Streicher et al. (2016) observed in similar small-scale experiments that bore interaction on the promenade can lead to amplified impacts, e.g. plunging bore breaking against the wall.

The blocking of the bore due to a wall on the promenade and the resulting impact of the bore against the wall is termed ‘wall effect’ by Chen et al. (2014). For a single bore overtopping the dike and impacting against the wall, they defined four stages of impact at the wall: In the (S1) pre-impact stage the bore was propagating and transforming over the promenade. During (S2) initial impact stage a first tiny water jet impacted at the wall. Followed by the main water wedge impact and squeezing of the initial water jet against the wall. This was followed by the (S3) deflection stage during which the water flipped through and was deflected upwards along the wall, transferring all kinetic energy into potential energy until maximum run-up at the wall was reached. Finally, during (S4) reflection stage the water started to fall downwards again, hitting the remaining incoming water and being reflected offshore again due to partial blocking of the wall.

Kihara et al. (2015) investigated Tsunami bore impacts on tide walls. Based on signals from pressure sensors measuring over the wall height, they distinguished four impact phases: (P1) Impulsive impact phase with a duration of 10^{-3} - 10^{-2} s. (P2) Dynamic impact phase, 0.1 - 1s long and during which the flow against the wall was fully developed and the water mass flipped upwards. (P3) Initial reflection phase during which the water collapsed on the continued incoming flow and pressures on the wall were larger than hydrostatic. (P4) Quasi-steady/hydrostatic phase from 10s after initial impact onwards during which the pressure distribution on the wall was hydrostatic.

The impact process for tsunamis (Kihara et al. 2015) and overtopping waves (Chen et al. 2014) are classified in various corresponding stages or phases, named differently and taking into account the differences between short duration overtopping waves and long duration tsunami bores.

Bore impacts against a vertical wall resulted in a double peak shape of the measured force impact signal (Ko et al. 2018; Van Doorslaer et al. 2017; Chen et al. 2015, 2014, 2012; Streicher et al. 2016; Kihara et al. 2015; De Rouck et al. 2012; Ramachandran et al. 2012; Ramsden 1996, Martin et al. 1999). The first peak was

129 typically assigned to a dynamic impact of the moving bore being blocked by the wall.

130 During deflection and reflection of the bore a dominant influence of the second
131 peak was observed. The physical reason for the second peak was discussed
132 controversially. It was either assigned to a hydrostatic force, due to the water in front of
133 the wall (De Rouck et al. 2012) or to the down-rush of water after run-up and blocking
134 of the wall in one direction (Streicher et al. 2016; Kihara et al. 2015; Chen et al. 2012;
135 Martin et al. 1999; Ramsden 1996). The latter argued that the second force peak was
136 situated after the maximum run-up in time and therefore cannot be directly assigned to a
137 maximum water layer in front of the wall. Kihara et al. (2015) assumed that the second
138 peak in the impact signal was due to two effects, acceleration of continuous flow
139 against the lower part of the wall and downward accelerated flow by gravity due to
140 collapsing water. The double peak impact signal shape was already described by
141 Kortenhaus et al. (1998) and Oumeraci et al. (1993) for direct wave loading of
142 structures situated in relatively deep water. Kortenhaus et al. (1998) defined a criterion
143 to classify the entire impact either as a dynamic (dominant first peak F_1) or quasi-static
144 (dominant second peak F_2) impact type. If the force ratio F_1/F_2 exceeds 2.5, the impact
145 would be considered a dynamic impact type.

146 Ko et al. (2018) for the first time described the double peak impact signal shape
147 theoretically and validated their assumption with measurements obtained from
148 experiments studying Tsunami bore impacts on building walls. With laser induced
149 fluorescence method they were able to cut out cross sections of the water body in front
150 of the wall to determine the splash-up height, which is a different term for run-up
151 height, at the wall in small-scale experiments. They observed a two-peaked impact
152 signal with the first peak related to the slamming action and rising water in front of the
153 wall and the second peak related to falling action and the collapsing of water after
154 maximum splash-up. The generated Tsunami bores were repeatable enabling a
155 statistical analysis of the parameters. Based on a very short duration observation
156 $2.72\ s < t < 2.8\ s$, where the impact pressure gradients are very small over the wall

height, they made the assumption that the velocity profile in front of the wall can be seen as uniformly distributed over the height. When using the Euler equation to predict the force response of the structure and assuming uniform velocity profiles, the measured force was better approximated than using the hydrostatic approach (which would always overestimate the impact force) based on splash-up height. The slight overestimation using the Euler equation might be a result that incompressible fluid is assumed in theory, while in the experiment a two-phase flow of air and water was present. Hence, the impact forces were reduced. In all cases using a uniformly distributed velocity profile resulted in better force estimates than using a linearly distributed velocity profile. Hence, they made the assumption that the splash-up water body, at least at the tip of the splash-up behaves like a solid body projectile.

OBJECTIVES

It is the aim of this study to extend the knowledge about overtopped bores impacting a dike-mounted vertical wall in shallow water and mildly sloping foreshore conditions. An identification of bore interaction patterns will be obtained based on the observed physical processes from laser scanner and video image data. This study also aims to further elaborate on the physical processes underlying short-duration bore impacts on a dike-mounted wall, based on pressure distribution and total horizontal impact force. A final goal is to develop a thorough methodology to classify the different impact types. More detailed objectives are:

(1) To increase the knowledge and understanding of short-duration overtopped bore impacts on dike-mounted vertical walls required for a reliable and safe design of these structures with respect to sea level rise and increased storminess in the future.

(2) To study overtopping bore interactions of multiple bores in vicinity of a dike, promenade and dike-mounted vertical wall in shallow water and mildly sloping foreshore conditions. The complexity of these processes and difficulty

of measurement due to alternating dry and wet conditions on the promenade requires innovative measurement techniques.

(3) To investigate bore impact processes on dike-mounted vertical walls in order to classify bore impact types.

(4) To discuss links between bore patterns and bore impact types and to elaborate on the implications on any prediction tools and scale effects.

Nomenclature

h	Water depth [m]	F	Total impact force [$kN \cdot m^{-1}$]
H_{m0}	Spectral wave height [m]	P	Impact pressure [kPa]
$T_{m-1,0}$	Spectral wave period [s]	z	Vertical location at wall [m]
$_t$	Subscript for dike toe location	t_r	Impact rise time [s]
$_o$	Subscript for offshore location	t_d	Impact duration [s]
g	Gravitational acceleration [$m \cdot s^{-2}$]	t_n	Resonance period structure [s]
θ	Foreshore slope [-]	$h_t/H_{m0,o}$	Relative water depth dike toe [-]
β	Surf-similarity parameter $= \tan(\theta)/\mathrm{sqrt}(H_{m0,o} \cdot 2 \cdot \pi/g \cdot T_{m-1,0,o})$	$S_{m-1,0}$	Wave steepness $= H_{m0} \cdot 2 \cdot \pi/g \cdot T_{m-1,0}^2$ [-]

EXPERIMENTAL SET-UP AND TEST PROGRAM

Model tests were conducted in March 2017 in the Delta Flume in Delft, The Netherlands, as part of the research project WALOWA (WAve LOads on WAlls). The model geometry was divided into four parts: (1) A sandy foreshore with a combined slope θ_1 = 1-to-10 at the beginning and θ_2 = 1-to-35 seaward of the toe of the dike, along reaches of 19.5 m and 61.6 m, respectively. The total foreshore volume was comprised of ~1000 m³ of sand spread over the 5 m flume width. (2) Attached to the foreshore a concrete dike with a 1-to-2 slope and (3) a 2.35 m-wide promenade with an offshore slope of 1-to-100 to drain the water. (4) At the end of the promenade a vertical 1.6 m-high steel wall was built to measure the impact pressures with pressure sensor mounted into a pressure plate (see Figure 2). The model dimensions are given in model scale using Froude length scale and scale factor 1-to-4.3. A more detailed description of the model and measurement set-up was given by Streicher et al. (2017).

[Figure 2]

For the purpose of this study two irregular wave tests, Irr_1_F and Irr_4_F,

205 comprised of 1000 waves each were selected (Table 2). The range of tested wave
206 parameters was similar to a design storm with 1000- and 17,000-year return period for
207 the Belgian coast (Veale et al. 2012). The values were reduced to model scale using a
208 Froude length scale factor of 1-to-4.3. The indices 't' and 'o' refer to the measurement
209 location at the dike toe (X=175.08 m from the paddle) and in the offshore (wave gauge
210 2, 3 & 4), before the start of the foreshore, respectively. The spectral wave parameters at
211 the dike toe were determined with validated SWASH model calculations (Streicher et
212 al. 2017). The offshore spectral wave parameters were obtained from reflection
213 analysis. As expected, the wave height decreased by a factor of 3.5 - 4.0 due to wave
214 breaking and loss in energy on the mild foreshore; and the spectral wave period
215 increased by a factor of 2.1 - 2.2 due to the release of the bound long waves in the
216 breaking process on the mild foreshore (Hofland et al. 2017). The offshore breaker
217 parameter β_o indicated spilling wave breaking, typical for mild foreshores and the wave
218 steepness at the dike toe $S_{m-1,0,t} < 0.01$ often means that the waves were broken due to
219 depth limitations (Eurotop 2016). The relative water depths at the dike toe $h_t/H_{m0,o}$ were
220 lower than 0.3 and considered extremely shallow (Hofland et al. 2017). The according
221 freeboards A_c, distance between SWL and the height of the promenade, ranged between
222 0.27 m and 0.47 m.

223 [Table 2]

224 For both selected tests, Irr_1_F and Irr_4_F the 30 highest impacts, according to
225 the maximum impact forces, were selected for the analysis. This resulted in 60 analyzed
226 individual impacts. With a total number of 760 (Irr_1_F) and 251 (Irr_4_F) detected
227 impacts, the analyzed impacts represent a relative sample size of 4% and 12% of the
228 total number of impacts, respectively for test Irr_1_F and test Irr_4_F. The 30 highest
229 force impacts were numbered in descending order based on the maximum peak of the
230 measured force signals. On one hand this was a relatively small sample to be
231 representative for all measured impacts, on the other hand this allowed us to focus more
232 on individual analysis of the highest impacts. The authors preferred to focus on the

analysis to the extreme events with the purpose of formulating practical and reliable design guidance. Inherent to this selection procedure was that the obtained 60 impacts were of rather random nature in terms of bore impact process and bore formation process prior to impact. The large variation of incoming bore parameters, e.g. bore interaction patterns required an individual analysis and process description for each individual impact event (see Figure 3). The measurement files were cut to 3-s-long clips for all 60 impacts to facilitate the analysis. In all cases the range extending from 1.5 s before to 1.5 s after the maximum impact force was considered for further analysis. [Figure 3]

ANALYSIS METHODS

This section comprises the methods to analyse the acquired data and an outline of the results for bore interaction patterns, bore run-up at the wall and bore impact types.

BORE INTERACTION PATTERNS

During wave breaking on the foreshore, run-up on the dike, overtopping over the dike crest and travelling across the promenade, until impact against the wall, waves experience several transformation processes. This results in broken waves, which propagate as “short-duration bores” (in contrast to the long- duration bores induced by tidal and tsunami bores) with different patterns and characteristics affecting the final impact loading of the wall. Due to the irregular nature of random sea waves, the short-duration bores overtake each other, collide with reflected bores, and exhibit a number of further interaction patterns over the entire length of the bore transformation area. To study the bore interaction processes in a nonintrusive way and in alternating wet and dry conditions on the promenade, high resolution profile measurements of the water surface with a SICK LMS511 laser profiler were obtained. The laser was mounted at the left flume sidewall (when standing with the back to the wave paddle), approximately 5 m above the dike toe location (Figure 4).

[Figure 4]

A slant angle of 23° was used to avoid a spiky signal due direct reflection at nadir (Hofland et al. 2015; Blenkinsopp et al. 2012). This resulted in a scanned profile approximately in the middle of the flume (~y = 2.7m), next to the pressure plate in the steel wall (see Figure 2). The measurement frequency was 35Hz with an angular resolution of 0.25°. The distance between scanned points is a function of the distance the laser beam had to travel and the angular resolution. On the promenade the average distance between individual scan points was 2.55 cm. The signal was synchronized with the other recordings via a synchronization pulse received from the main data acquisition system. There are several issues related to the reflection characteristics of the (foamy) water and laser beam characteristics (Hofland et al. 2015). The mostly foamy water surface of the turbulent bores resulted in good reflection characteristics with a sufficiently high received signal strength indicator (RSSI). This indicated that the turbidity of the water did not play a role as the foam was much more reflective and the penetration of the laser beam into the water was absent with foam. Hence, a better accuracy than the estimated range precision (standard deviation) of 1-1.5 cm found by Streicher et al. (2013) was assumed. The range precision was determined for incidence angles of 15°-90° (angle between incident laser beam and still water surface) in the direction of the laser beam. In parts were there was no foam on the water, the turbidity much lower than 40 NTU (Blenkinsopp et al. 2012) and the distance between water surface and laser profiler not low enough to provide sufficient reflection strength, no water surface measurement was obtained (e.g. second row in Figure 7, A). Profile measurements covered the water surface at offshore of the dike toe, the dike, promenade until the wall and in total a horizontal length of ~21 m. This resulted in a field of view of 114°. To distinguish the different bore formation patterns, the high spatial and temporal laser scanner measurement related to each impact event were analyzed together with the video side- and overview images. This resulted in 5 observed bore patterns: (1) *regular bore pattern*, (2) *collision bore pattern*, (3) *plunging breaking bore*

pattern, (4) *sequential overtopping bore pattern*, and (5) *catch-up bore pattern* (see Figure 5).

[Figure 5]

The *regular bore pattern* (1) consists of a single turbulent bore travelling over the foreshore and approaching the dike. This bore overtopped the dike, travelled along the promenade and impacted on the wall without interaction with previous bores (see Figure 6, A). These types of bore patterns mostly occurred in test ID Irr_4_F with the less energetic wave conditions.

The collision bore pattern (2) refers to the situation of an incoming bore which collided with a previously reflected bore (see Figure 6, B). The reflection of the previous bore took place at the dike or at the wall. The next incoming bore collided with the reflected bore and broke again. This resulted in a loss of bore front uniformity, as well as air and turbulence induced due to the breaking process. The subsequent overtopping and impact at the wall was expected to be lower than for the *regular bore pattern*. If the collision occurred on the promenade, usually the incoming bore jumped over the reflected bore. If the collision took place in vicinity of the wall, this resulted in *plunging breaking bore pattern* (3). Breaking against the wall and inclusion of an air pocket between breaking bore and wall are the characteristics of this bore type. Entrapped air due to plunging breaking against a wall was also observed by Oumeraci et al. (1993) for breaking wave impacts in deep water conditions, and this introduces a problematic issue related to scaling of impact forces.

[Figure 6]

The sequential overtopping bore pattern (4) was an overtopping bore which slides on a residual water layer on top of the promenade, remaining from previous overtopping events (see Figure 7, A). There was no collision with reflected bores observed, but instead delayed breaking of the incoming bore on the residual water layer on the promenade and a highly turbulent bore front which slid on top of the residual water layer was observed until the bore impacted the wall. The friction between

315 incoming bore and promenade was reduced due to the residual water layer and the
316 impact at the wall was expected to be of higher magnitude.
317 *The catch-up bore pattern (5)* was observed for two successive bore crests with different
318 velocities travelling over the foreshore and approaching the wall (see Figure 7, B).
319 While travelling on the foreshore and overtopping the dike, the second bore crest
320 travelled faster and overtook the slower first bore crest. If the first bore broke against the
321 dike, it further facilitated the catch-up of the second bore. Also, this resulted in an
322 enhanced overtopping mechanism because the first bore would cushion the breaking
323 against the dike of the incoming second bore and less energy was lost during the
324 overtopping process of the second bore. The relatively higher velocity of the second
325 bore accelerated the water mass in the first bore along the promenade and higher energy
326 impacts occurred.
327 [Figure 7]
328 As can be seen from the catch-up pattern, all bore patterns are often influenced
329 by another mechanism, termed *efficient overtopping mechanism*. *Efficient overtopping*
330 *mechanism* was observed when there was a sufficiently high water level in front of the
331 dike due to previous waves and wave set-up. During *efficient overtopping mechanism*
332 the incoming wave would not break against the dike but instead approaches at the same
333 height as the dike crest and overtops the dike very smoothly. *With efficient overtopping*
334 *mechanism* there was no energy lost due to breaking of the incoming bore against the
335 dike; therefore, it was expected that the *efficient overtopping mechanism* also increases
336 the impact force on the wall. This is in contrast to an emerged dike against which the
337 incoming bore breaks and loses part of its energy due to the breaking process. A series
338 of bore patterns were sometimes visible prior to one impact event. For this study, it was
339 decided to identify only one bore pattern which was visually more distinct. Also,
340 complex 2D effects (non-uniform flow in cross flume direction), foamy bore fronts and
341 air entrainment during breaking, were observed and are expected to change the impact

342 characteristics of the bore against the wall.

343 ***RUN-UP AT WALL***

344 In addition to the measured pressures and total impact forces, a hydrostatic
345 pressure estimate was derived based on the instantaneous run-up of the bore at the wall.
346 The instantaneous hydrostatic pressure estimate $P_{hyd}(t,y)$ was calculated for each
347 pressure sensor location y based on the instantaneous run-up $R_h(t)$ using the following
348 equation 1:

$$P_{hyd}(\mathrm{t},\mathrm{y}) = \rho \cdot g \cdot [R_h(t) - y] \quad (1)$$

349 The instantaneous run-up $R_h(t)$ of the impacting bore at the wall was determined
350 using two GoPro Hero5 video images from a side mounted and top mounted camera
351 and motion tracking of the leading edge of the run-up water body. The sampling rate
352 was 59.94 frames per second with a resolution of 2.7k (2704px·1520px). The spatial
353 resolution was always smaller than 2 mm in the areas of interest (wall, promenade and
354 dike). Line mode to automatically correct for the fish eye effect, resulting from lens
355 distortion of the GoPro camera, was enabled. Synchronization was achieved by using
356 red LEDs within the field of view which were giving a light pulse together with the
357 start of the main data acquisition system. The images from the overview camera (see
358 Figure 8, left) were used to track the leading edge of the run-up bore at the wall and
359 the images from the side view camera (see Figure 8, middle) to judge whether the run-
360 up water was in visible contact with the wall and where it separated because of
361 reflection from the wall. Therefore, only the area which was in visible contact with
362 the wall was used to determine the instantaneous run-up height. A length scale was
363 introduced to the images by measuring the length of defined objects in the images,
364 such as the 1.6-m wall height, and converting the obtained pixels into meters.

365 [Figure 8]

366 The red circles (see Figure 8, right) correspond to the same time stamps shown in the
367 overview (see Figure 8, left) and sideview (see Figure 8, middle) image. The run-up

was obtained on a line parallel to the pressure sensor array on the silver metal plate (see Figure 8 middle). According to the coordinate system in Figure 2, this corresponded to y = 2.15 m from the right flume wall (when standing with the back to the paddle). It was important to determine pressure and run-up measurement at the same location to take into account that the bore front was not always uniform along the flume width (e.g. cross waves, 2D effects along the flume width). Then the leading edge of the bore during the entire image sequence of impact and run-up was manually tracked in the video images and in this way the run-up at the wall was obtained.

The method of tracking the run-up leading edge in combined overview and sideview video images was preferred over obtaining the run-up, e.g. by using the highest pressure sensor that was showing an impact pressure in the wall, due to higher spatial resolution. Theoretically the accuracy of this method is determined by the spatial (2 mm resolution) and temporal (59.94 frames per second) resolution of the camera images. Nevertheless, the foamy and non-uniform bore front made it difficult to always identify the leading edge of the run-up bore. Hence, errors due to flow separation from the wall and fuzzy run-up front, are expected. A standard deviation for the maximum run-up $\sigma_{Rh,max}$ = 0.033 m was obtained by repeated tracking of the same event. This was equivalent to a relative error of 3% in terms of maximum run-up height $R_{h,max}$.

BORE IMPACT LOADS

The impact pressures were measured with 15 Kulite HKM-379 (M) pressure sensors spaced vertically and horizontally over a metal pressure plate (see Figure 2). The metal pressure plate was screwed into the opening and was flush-mounted with the steel wall as a result. The measurement range was 1 bar (0 to 100 kPa). The combined error due to non-linearity, hysteresis and repeatability compared to the best-fit straight line (BFSL) was stated to be typically smaller than 0.1% of the full scale output (FSO).

As a maximum it was stated that it never exceeds +-0.1% of the full scale output (FSO). The measurement frequency for pressure sensors was 1000 Hz. It was assumed that 1000-Hz sampling frequency was high enough to capture the short duration impulsive impacts (Schmidt et al. 1992). Post processing of the individual pressure sensor signals involved removing low frequency trends and applying a zero-offset correction to the signal. The filtering was done in the frequency domain and only the electrical noise around 50 Hz was removed from the pressure sensor signal. The post-processed and filtered individual pressure sensor signals were integrated over the height of the pressure array using rectangular integration method, and the result was given as a force per unit horizontal wall width [kN/m]. The integrated pressure over the height of the wall is further termed total impact force in this study. Finally, a half-automatic peak selection method was applied to determine the maximum total impact force for each of the 60 events (see Figure 9). The repeatability of the impact force estimate was dependent on the measurement accuracy, flow uniformity across the flume width, small air fluctuations in the impacting flow, etc. Previously the repeatability of impact forces resulting from a regular wave train in small-scale experiments was estimated with a coefficient of variation C_v in the range of 10% - 14% (Chen 2016).

[Figure 9]

The maximum total impact force for testID Irr_1_F was found to be 4.77 kN/m in model scale (88.2 kN/m in prototype using Froude length scale and a scale factor 1-to-4.3). The maximum total impact force for Irr_4_F was found to be 1.01 kN/m in model scale (18.7 kN/m in prototype using Froude length scale and a scale factor 1-to-4.3).

RESULTS AND DISCUSSION

Based on the measured total impact force and pressure distribution over the wall height, the characteristics of the impact signal were discussed. The combined evidence of visual process observations, total impact force and pressure distribution, were used to

422 classify impact types. Typically, the total horizontal impact force signal showed a
423 double peak shape for each impact event. While the first peak (F_1) was related to the
424 dynamic impact of the bore against the wall, the second peak (F_2) was related to the
425 down-rush of the bore after maximum run-up. For the investigated impacts in the
426 present study, the ratio of F_1/F_2 was in the range of 0.48 – 2.38. Using the classification
427 from Kortenhaus and Oumeraci (1998) for *church roof impact profiles* none of the
428 studied impacts were considered dynamic. Hence, the term *Twin Peaks* was preferred
429 for this situation, accounting for the fact that the magnitude difference of first (F_1) and
430 second (F_2) impact was smaller. For the present study the ratio F_1/F_2 impact = 1.2 was
431 used to distinguish *dynamic* ($F_1>1.2\cdot F_2$) and *quasi-static impact types* ($F_1<1.2\cdot F_2$). The
432 factor 1.2 was selected based on a comparison of the 30 highest impacts from test
433 Irr_1_F with the 30 highest impacts from a repetition test of Irr_1_F using the same
434 time-series of waves and geometrical set-up. The average difference between the 30
435 highest impacts was 0.39 kN/m. This was equal to an average difference in horizontal
436 impact force of 16%. In order to establish a robust distinction between first (F_1) and
437 second (F_2) impact, the 1.2 threshold, accounting for 20% variability in maximum
438 impact force, was chosen as a safe choice well above the measured 16%. In several
439 cases, the rise time $t_{r,F1}$ of the dynamic first (F_1) impact was very short ($t_{r,F1} = 3\cdot10^{-3}$ –
440 $1.2\cdot10^{-2}$s), comparable to impulsive impact phase duration 10^{-3}-10^{-2} s observed by
441 Kihara et al. (2015). The rise time in this study was defined as the time between the
442 start of the impact until the maximum recorded force. Hence, a second criterion was
443 introduced based on the rise time $t_{r,F1}$ of the first peak (F_1) to account for the possibility
444 of very short duration impulsive impact types. If the rise time of the first impact (F_1)
445 was shorter than $t_{r,F1} = 10^{-2}$ s the impact was considered *impulsive impact type*.
446 Furthermore, the *impulsive impact types* showed a very localized maximum pressure in
447 the lower part of the wall. The classification of impact types does not consider the
448 resonance period of the wall, since this is a very structure dependent parameter. In this

449 study only the loading conditions are investigated but not the structural response and the
450 criteria to determine the impact types are summarized in the methodology chart (see
451 Figure 10).
452 [Figure 10]

453 *Impulsive impact type*
454 For 9 of the studied 60 impacts a high magnitude and short duration ($t_r = 3*10^{-3}$ –
455 $1.2*10^{-2}$ s) peak in the beginning of the impact signal occurred (see Figure 11, middle),
456 resulting from the initial impact of the bore tip with the wall. It can be seen from the
457 sideview image (see Figure 11, left), that the upward deflection of the main water body
458 had not begun at this moment. From the pressure distribution (see Figure 11, right) it is
459 evident that the peak pressure was almost solely recorded at the second lowest pressure
460 sensor, indicating a highly localized phenomenon in the lower part of the wall.
461 [Figure 11]
462 A possible generation mechanism was either a very steep bore front which
463 impacted at the wall or when an incoming bore collided with a previously reflected bore
464 (tip) in vicinity of the wall under inclusion of an entrapped air pocket (e.g. Impact nr. 2
465 of test Irr_4_F). The latter resulted in plunging type bore breaking against the wall and
466 led to significantly higher impulsive impacts and an oscillating force signal due to the
467 oscillating entrapped air bubble (Bullock et al. 2007). Hence, they were referred to as
468 *impulsive impact types* and occurred over the entire spectrum of investigated impacts
469 with the second largest impact (F = 4.25 kN/m) classified as *impulsive impact type* (see
470 Table ANNEX 1 and ANNEX 2).

471 *Dynamic impact type*
472 After the initial *impulsive impact type* or in the absence of an *impulsive impact type*, the
473 continuous instream of water against the wall led to upward deflection of the water at the
474 wall and an increase in measured total force and pressures over the wall height (see

475 Figure 12, B). Usually this resulted in the first peak (F_1) in the measured *twin peaks* total
476 force signal. The measured pressures over the wall height were of larger magnitude than
477 the hydrostatic pressure based on the run-up at the wall, but smaller in magnitude than
478 any impulsive peak pressure. The pressure distribution was not linear but rather uniform
479 from the bottom up to about the 0.23 m wall height. Above 0.23 m wall height the drop
480 of pressures was more rapid with increasing height. It was assumed that the formation of
481 two rollers in the impacting flow result in this particular pressure distribution (Kihara et
482 al. 2015). An outward directed roller above 0.23 m in counterclockwise direction (in
483 reference to the sideview frame shown in Figure 2), resulted in the rapid pressure drop.
484 Conversely, the flow formed a clockwise roller below 0.23 m wall height, resulting in
485 downward acceleration in the lower part of the wall and the expected hydrostatic
486 decrease was compensated by this downward accelerated water body. This led to the
487 assumption that the dynamic effects based on incoming bore velocities and their change
488 in direction were dominant over the hydrostatic effects at this moment. Hence, the first
489 impact (F_1), in the absence of an *impulsive impact type*, was termed *dynamic impact type*.
490 At first it seems difficult to distinguish *impulsive and dynamic impact types* and there
491 were usually components of both impact types present. However, while the rise time of
492 the *impulsive impact types* was of very short duration ($t_r = 3*10^{-3} – 1.2*10^{-2}$ s) and highly
493 localized in terms of pressure distribution on the wall (see Figure 11), the *dynamic*
494 *impact types* showed longer rise times t_r of the maximum total impact force (0.1 – 0.6 s).
495 Also, the high impact pressures were distributed over a larger area at the wall.
496 [Figure 12]

497 *Dynamic impact types* were found over the entire magnitude spectrum of the
498 studied impacts. The fourth largest impact (F = 4.21 kN/m) was classified as dynamic
499 impact type (see Table ANNEX 1 and ANNEX 2).

500 After the peak of the dynamic impact force, the water was continuously
501 deflected upwards until it reached the elevation of maximum run-up at the wall (see

Figure 12, B). At the same time the measured pressures over the entire wall height were smaller than the hydrostatic pressure estimate. Still, a small uniform pressure distribution in the lower part of the wall below y = 0.16 m could be observed. It was assumed that a small portion of the clockwise roller is still present in this lower region at the wall. The original expectation would be that the measured pressures and total force were close to the hydrostatic force and pressure estimate at the moment of maximum run-up. This was not observed and the measured pressure distribution and total force over the wall height showed lower values (see Figure 12, C). It was assumed that this difference arose from the different vertical accelerations in the run-up water body. As the rising water velocity decreased to zero, an upward-directed acceleration made it appear as if the water mass had less than its actual weight. Thus, the measured force was reduced from what the hydrostatic force would be because the "apparent weight" of the water was less than the actual water weight. We hypothesize that the change in pressure over a small length of the vertical wall at the moment of maximum run-up consists of the hydrostatic pressure due to gravity minus the pressure due to the positive upward acceleration of the run-up. The pressure gradients were rather large in this study, thus leading to the assumption that velocities were not uniform over the wall height. Hence, the water body experiences acceleration in vertical direction. The magnitude of the upward acceleration depends on the temporal and spatial variation of vertical velocity of the run-up flow. High resolution velocity and acceleration measurements of the bore flow at the wall would be required to further investigate.

Quasi-static impact type

After maximum run-up of the water body at the wall, the upper part of the water body collapsed; and due to blocking of the wall, outward reflection of the water body occurred. A short time after the maximum run-up, the pressures in the upper part of the water body were larger than estimated hydrostatic pressures based on the instantaneous run-up (see Figure 12, D). It was hypothesized that this difference was also related to

529 the vertical accelerations of the water body in front of the wall. The falling water
530 velocity approached zero, and a downward-directed acceleration added to the effect of
531 gravitational acceleration giving an apparent water weight greater than the actual
532 weight. The magnitude of the downward acceleration was dependent on the time and
533 spatial variation of vertical velocity. Despite the small additional dynamic component,
534 the pressure distribution resembled a hydrostatic distribution and the measured total
535 force almost fell together with the hydrostatic force estimate based on the instantaneous
536 run-up of the water at the wall (see Figure 12, D). Hence, the authors decided to use the
537 term *quasi-static impact type* to refer to the second peak (F_2) in the impact signal
538 because of the dominant hydrostatic effects. The small dynamic component is
539 sufficiently considered by using the term "quasi" in the impact type name. *Quasi-static*
540 *impact types* comprised the majority, as well as the largest (F = 4.77kN/m),
541 investigated impacts (see Table ANNEX 1 and ANNEX 2).

542 Unlike tsunami bore impacts, which reach a quasi-steady state a few seconds
543 after the main impact (Kihara et al. 2015), this was never really the case for the short
544 duration bore impacts examined in the present study. However, the total horizontal
545 force converged with the hydrostatic force estimates and the estimated hydrostatic
546 pressure line with the measured pressures towards the tail of the impact time series (see
547 Figure 12, E).

548 As a summary, the combined impacts from test Irr_1_F and Irr_4_F were
549 classified as *impulsive* in fifteen percent and in *dynamic impact types* in fifteen percent
550 of the impacts as well. The *quasi-static impact types* were found in seventy percent or
551 ~2/3 of the impact events (see Figure 13, right). There were fewer *dynamic impact types*
552 for test Irr_4_F compared to Irr_1_F. At the same time the number of *impulsive impact*
553 *types* increased for test Irr_4_F, while the *quasi-static impact types* remain almost
554 constant in number. This is attributed to the fact that the overtopped water volumes
555 were of smaller thickness and duration for test Irr_4_F, such that a full dynamic impact

with continuous instream of water and formation of rollers could not develop. Given the fact that the majority of impacts (~2/3) and the largest impacts were of *quasi-static impact types*, they were considered as the most relevant impact type to be further investigated.

[Figure 13]

The non-dimensionalized impact force showed that below $F/\rho \cdot g \cdot R_{h,max}^2 = 0.5$ all the *quasi-static impact types* were found (see Figure 13, left). The best-fit line through this part of the data was at $F/\rho \cdot g \cdot R_{h,max}^2 = 0.32$, which indicated that a prediction for these impacts could be achieved using hydrostatic theory, the maximum run-up $R_{h,max}$ and a coefficient 0.32. In between $0.5 < F/\rho \cdot g \cdot R_{h,max}^2 < 0.9$ only *dynamic and impulsive impact types* were found and above $F/\rho \cdot g \cdot R_{h,max}^2 > 0.5$ only *impulsive impact types* were found.

LINK BETWEEN BORE IMPACT TYPES AND BORE INTERACTION PATTERNS

Only the *plunging bore pattern*, collision of incoming with reflected bore in vicinity of the wall and breaking under entrapped air against the wall, resulted in *dynamic/impulsive impact types at all times* (see Figure 14). Similar findings are reported for plunging type wave breaking against a vertical sea wall (Oumeraci et al. 1993). For the other bore patterns (*regular, catch-up, collision and sequential bore pattern*) the link between the pattern and impact type at the wall was not as apparent as for the *plunging breaking bore pattern*. Most of the bore patterns (46% of events or 28 in total), were comprised of *collision bore patterns*. From which the majority of events (23 out of 28 events) resulted in *quasi-static impact types*. The same trend was observed for *catch-up (16% of events or 10 in total), sequential (13% of events or 8 in total), regular bore interaction pattern (17% of events or 10 in total),* with most of them resulting in *quasi-static impact types* (see Figure 14). When considering *efficient overtopping mechanism*, i.e. when the water at the dike was sufficiently high for the

583 next incoming bore to just pass over the dike crest without breaking against the dike, it
584 was observed that the bores were more likely to generate a *dynamic* or *impulsive impact*
585 *type*; e.g. taking into account *efficient overtopping mechanism* for the *collision bore*
586 *pattern*, 80% of the bores generated a *dynamic/ impulsive impact type*. On the contrary,
587 without *efficient overtopping mechanism* the collision bore pattern generated a *quasi-*
588 *static impact type* in 95% of the cases. This yields to the conclusion that with *efficient*
589 *overtopping mechanism* sufficient energy in the overtopping bore is maintained, and not
590 dissipated during wave breaking against the dike, resulting in larger *dynamic impacts*
591 (F_1) on initial impact compared to the *quasi-static impacts* (F_2). Only for test Irr_4_F
592 (see Table 2), with less energetic hydrodynamic conditions, *regular bore patterns* were
593 observed. For this bore pattern, the absence of interaction, leading to bore breaking,
594 with other bores was the key criterion. No interaction mainly resulted from the fact that
595 the overtopped bores were less in total number and shorter in duration for test Irr_4_F
596 with lower overtopping discharge compared to test Irr_1_F.
597 [Figure 14]
598 The findings are an extension of the results from Chen (2016), who identified *catch- up,*
599 *collision* and *plunging bore pattern* as well as single wave pattern, equivalent to the
600 regular bore pattern in the present study. However, the *sequential bore pattern and*
601 *efficient overtopping mechanism* are introduced for the first time in the present study,
602 *collision and catch-up bore pattern* already observed before the dike, the probability of
603 occurrence discussed and a first attempt to link the bore interaction patterns to the
604 impact types attempted.

605 ***IMPLICATIONS OF IMPACT TYPES AND BORE PATTERNS ON FORCE***
606 ***PREDICTION UNDER CONSIDERATION OF SCALE EFFECTS***

607 Bore interaction patterns resulting from broken irregular waves were observed to
608 increase the turbulence, aeration and flow complexity of the incoming flow.
609 Furthermore, bore thickness and velocity changed dramatically along the promenade,

610 e.g. when *catch-up bore pattern*, *plunging bore breaking* or *collision bore pattern*
611 occurred. Hence, it was concluded that for maximum impacts the flow parameters bore
612 thickness and velocity are a less reliable predictor of impact forces. Any prediction tool
613 derived from measurements of bore thickness and velocity on the promenade and used
614 for the prediction of maximum impact forces should therefore be treated carefully. It
615 was concluded that a deterministic prediction of the maximum impact force based on
616 the process parameters run-up at the dike, overtopping of the dike, bore thickness and
617 velocity on the promenade can hardly be achieved due to the presented bore interaction
618 patterns. Furthermore, small variations during bore transformation along the
619 promenade, bore front uniformity, air entrainment, 2D effects and the turbulent flow
620 processes in vicinity of the wall complicate any deterministic prediction of maximum
621 impact forces. Additionally, most of the impact prediction tools suffer from the
622 drawback that they are not designed for a geometrical set-up with dike mounted vertical
623 walls. E.g. impact prediction force formula in U.S. Army Corps of Engineers (2002),
624 based on the works by Camfield (1991), are designed for land based structures on a
625 plane slope not taking into account overtopping over the dike crest in extremely shallow
626 waters. If they are designed to predict impact forces on dike mounted walls in extremely
627 shallow waters, they often predict average impact forces (e.g. Van Doorslaer et al.
628 2017; Kortenhaus et al. 2016; Chen et al. 2015) or a maximum impact force but do not
629 account for the different physical processes resulting in the different impact types
630 (summary given in Streicher et al. 2018). Maximum impact forces are key for a reliable
631 design of coastal structures and often derived from small-scale experiments and up-
632 scaled to prototype. In this way they suffer from scale-effects, mainly due to
633 dissimilarities in the entrained air and the air content of the foamy bores (Blenkinsopp
634 et al. 2007). Entrained air usually leads to cushioning effects of the impact pressures.
635 Hence, less air entrained in the small-scale experiments will lead to less cushioning of
636 the impact (Bullock et al. 2001). This is expected to lead to an overestimation of the
637 impact loads, when upscaling the results from small-scale to prototype (Cuomo et al.

2010). Here, the classification into impact types gives useful insights. Mainly the very short duration and localized *impulsive* and also the *dynamic impact types* are expected to suffer from scale-effects when up-scaled to prototype due to the not properly scaled air properties and cushioning effects in the impacting flow. On the contrary *quasi-static impact types* are expected to be less affected by scale-effects, due to the almost hydrostatic situation of the water in front of the wall after maximum run-up. Since the total impact force signal showed a *Twin Peaks* shape, with similar magnitudes of *dynamic* (F_1) and *quasi-static impact type* (F_2), the majority of impacts (~2/3) and largest impact force (see Table ANNEX1 and ANNEX2) were considered *quasi-static impact type*, it might be worthwhile to consider only *quasi-static impact types* for the structural design. This is strictly only possible if no dynamic effects, due to the natural period of the structure t_n being in the range of impact rise times t_r, need to be considered (see Figure 10). Typically natural periods of 3-50 m high buildings are in the range of 0.1 - 1s (Chen 2016). The studied rise times for *impulsive impact types* ($tr_{,F1} = 3*10^{-3}$ – $1.2*10^{-2}$ s) did not fall within this range. This becomes different if there are e.g. glass structures with higher natural periods. Anyhow, the rise times of the *dynamic impact types* (0.1 – 0.6 s) where in the critical range and dynamic structural analysis most likely has to be carried out.

CONCLUSION AND OUTLOOK

The complex interaction of short-duration bores resulting from irregular broken waves in extremely shallow waters were studied, and the types of bore interaction patterns were identified. The impacts the bore generated at the vertical wall were classified into three impact types, and a link between bore patterns and impact types was discussed. This study focused on the 60 highest bore impacts on a vertical wall for 2 tests (30 impacts from each test) with wave steepness's at the dike toe of 0.0012 and 0.0014 as well as an offshore breaker parameter of 0.2 (similar to design storm conditions at the Belgian coast with a 1000-year and 17000-year return interval).

665 The results and conclusions can be summarized as followed:

666 (1) Five bore interaction patterns prior to impact were identified: (1) *regular bore*
667 *pattern*, (2) *collision bore pattern*, (3) *plunging breaking bore pattern*, (4)
668 *sequential overtopping bore pattern* and (5) *catch-up bore pattern*. The bore
669 interaction process complicates a deterministic prediction of impact forces
670 based on bore properties, e.g. thickness and velocity.

671 (2) For the bore impacts at a dike mounted vertical wall a double peak impact signal
672 shape was observed, with similar magnitudes for the two peaks. A classification
673 methodology was developed and three bore impact types were distinguished: (1)
674 *impulsive impact type*, (2) *dynamic impact type*, (3) *quasi- static impact type.*

675 (3) A majority of impacts (~2/3 of all impacts) and the largest impact force was
676 considered *quasi-static impact type*. Based on this findings it was suggested to
677 use the *quasi-static impact types* to derive a maximum force estimate for
678 structural design guidance. This would have the advantage that the up-scaled
679 results are less affected by scale effects due to the almost hydrostatic behavior of
680 the water in front of the wall for this impact type. This is strictly only possible if
681 no dynamic effects, due to the resonance period of the structure t_n being in the
682 range of the impact rise time t_r, need to be considered for structural analysis.

683 (4) A link between the five identified bore patterns and the three identified impact
684 types was discussed. Only p*lunging bore pattern* lead to *dynamic/impulsive*
685 *impact types* in any case. *Collision bore pattern* was the most frequent (46% of
686 all interaction patterns were identified as *collision bore pattern*) and resulted in
687 *quasi-static impacts type* in a majority of cases. The other bore patterns were
688 equally frequent and most of them resulted in *quasi-static impact type.*

689 (5) A more practical conclusion was that the maximum measured impact force for
690 extremely shallow foreshore conditions, wave steepness $S_{m-1,0,t} = 0.0012$ and
691 breaker parameter $\beta_o = 0.02$ (similar to a design storm condition with a 1000-

692 year return interval at the Belgian coast) showed a maximum expected impact
693 force of ~19 kN/m (prototype value).
694 Though experiments were conducted at rather large scale (Froude length scale factor 1-
695 to-4.3), scale effects are still expected, mainly due dissimilarities in the entrained air
696 and the air content of the foamy bores, when upscaling the obtained results to
697 prototype, especially for the measured impact pressures and the resulting impact forces
698 of the *dynamic and impulsive impact types*. A further investigation of the entrained air
699 in the overtopping bores and consequent scale effects for overtopped wave impacts in
700 extremely shallow water conditions is therefore required. Additionally, an advanced
701 study of bore transformation parameters, such as bore front slope, bore thickness and
702 velocity in vicinity of the wall for single impact events related to regular bore
703 interaction patterns would increase understanding of the *impulsive and dynamic impact*
704 *types*. A statistical analysis to predict the maximum impact force of overtopped bores
705 on a dike mounted vertical walls might be more beneficial to account for the stochastic
706 behavior of the measured impacts.

707 **REFERENCES**

708 Blenkinsopp, C., Turrner, I.,L., Allis, M.,J., Peirson, W.L., Garden, L.,E., 2012.
709 Application of LiDAR technology for measurement of time-varying free-surface
710 profiles in laboratory wave flume. Coastal Engineering, Vol. 68, p. 5.
711 Blenkinsopp, C.E., Chaplin, J.R., 2007. Void fraction measurements in breaking waves.
712 *Proceedings of the Royal Society A: Mathematical, Physical and Engineering*
713 *Sciences*, Vol. 463 (2088), pp. 3151-3170. doi**:** 10.1098/rspa.2007.1901.
714 Bullock, G.N., Obhrai, C., Peregrine, D.H., Bredmose, H., 2007. Violent breaking wave
715 impacts. Part 1: Results from large-scale regular wave tests on vertical and sloping
716 walls. Coastal Engineering, Vol, 54, pp. 602-617.
717 Bullock, G. N., Crawford, A.R., Hewson, P.J., Walkden, M.J.A., Bird, P.A.D., 2001. The
718 influence of air and scale on wave impact pressures. Coastal Engineering, Vol. 42
719 (4), pp. 291-312, doi: 10.1016/S0378-3839(00)00065-X.

720 Camfield, F.E., 1991. Wave Forces on Wall. Journal of Waterways, Ports, Coastal and
721 Ocean Engineering, Vol. 177 (1), pp. 76-79, doi: 10.1061/(ASCE)0733-
722 950X(1991)117:1(76).
723 Cappietti, L., Simonetti, I., Esposito, A., Streicher, M., Kortenhaus, A., Scheres, B.,
724 Schuettrumpf, H., Hirt, M., Hofland, B., Chen, X., 2018. Large-scale experiments
725 of wave-overtopping loads on walls: Layer thicknesses and velocities. 37th
726 International conference on ocean, offshore and arctic engineering, Madrid, Spain,
727 p. 6.
728 Chen, X., 2016. Impacts of overtopping waves on buildings on coastal dikes. PhD thesis.
729 doi: 10.4233/uuid:e899b6e4-fcbe-4e05-b01f-116901eabfef.
730 Chen, X., Hofland, B., Altomare, C., Suzuki, T. and Uijttewaal, W., 2015. Forces on a
731 vertical wall on a dike crest due to overtopping flow, Coastal Engineering, Vol.
732 95, pp. 94-104.
733 Chen, X., Hofland, B., Altomare, C., Uijttewaal, W., 2014. Overtopping flow impact on a
734 vertical wall on a dike crest. 34th International conference on coastal engineering,
735 Seoul, Korea, p. 10.
736 Chen, X., Uijttewaal, W.S.J., Verhagen, H.J., Jonkman, S.N., Verwaest, T., Hassan, W.,
737 Suzuki, T., 2012. Hydrodynamic load on the building caused by overtopping
738 waves, Proceedings of 33rd International conference on coastal engineering,
739 Santander, Spain, p. 11.
740 Cooker, M, Peregrine, D., 1995. Pressure-impulse theory for liquid impact problems.
741 Journal of Fluid Mechanics, Vol. 297, pp. 193-214.
742 doi:10.1017/S0022112095003053
743 Cuomo, G., Allsop, W. and Takahashi, S., 2010. Scaling wave impact pressures on
744 vertical walls. Coastal Engineering, Vol. 57, pp. 604-609.
745 De Rouck, Van Doorslaer, K., Versluys, T., Ramachandran, K., Schimmels, S., Kudella,
746 M., Trous, K., 2012. Full scale impact tests of an overtopping bore on a vertical
747 wall in the large wave flume (GWK) in Hannover. 33rd International conference
748 on coastal engineering, Santander, Spain, p. 11.
749 EurOtop, 2016. Manual on wave overtopping of sea defences and related structures. Van
750 der Meer, J.W., Allsop, W., Bruce, T., De Rouck, J., Kortenhaus, A., Pullen, T.,
751 Schüttrumpf, H., Troch, P., Zanuttigh, B.
752 Hofland, B., Chen, X., Altomare, C., Oosterlo, P., 2017. Prediction formula for the
753 spectral period Tm-1,0 on mildly sloping shallow foreshores, Coastal Engineering
754 123, 21-28.

Hofland, B., Diamantidou, E., Steeg, P.v., Meys.,P., 2015. Wave run-up and wave overtopping measurements using a laser scanner. Coastal Engineering, Vol. 106, pp. 20-29.

IPCC, 2014: Climate Change 2014: Synthesis Report. Contribution of Working Groups I, II and III to the Fifth Assessment Report of the Intergovernmental Panel on Climate Change [Core Writing Team, R.K. Pachauri and L.A. Meyer (eds.)]. IPCC, Geneva, Switzerland, 151 pp.

Kihara, N., Niida, Y., Takabatake, D., Kaida, H., Shibayama, A., Miyagawa, Y., 2015. Large-scale experiments on tsunami-induced pressure on a vertical tide wall. Coastal Engineering, Vol. 99, pp. 46-63, doi: 10.1016/j.coastaleng.2015.02.009.

Ko, H. T.-S., Yeh, H., 2018. On the splash-up of tsunami bore impact. Coastal Engineering, Vol. 131, p. 11. doi: 10.1016/j.coastaleng.2017.10.002.

Kortenhaus, A., Gallach Sanchez, D., Streicher, M., Hohls, C., Trouw, K., Altomare, C., Suzuki, T., Thoon, D., Troch, P., De Rouck, J., 2017. Wave Overtopping and Wave-induced Loads on Coastal Sea Walls. Coastal structures and solutions to coastal disaster joint conference, Boston, USA, p. 7.

Kortenhaus, A. and Oumeraci, H., 1998. Classification of wave loading on monolithic coastal structures. 26th International conference on coastal engineering, Copenhagen, Denmark, pp. 867-880.

Lubin, P., Chanson H., 2017. Are breaking waves, bores, surges and jumps the same flow?. Environmental Fluid Mechanics 17 (1), 47-77. doi: 10.1007/s10652-016-9475-y.

Martin, F.L., Losada, M.A. and Medina, R., 1999. Wave loads on rubble mound breakwater crown walls. Coastal Engineering, Vol. 37, pp. 149-174.

Oumeraci, H., Klammer, P. and Partenscky, H., 1993. Classification of breaking wave loads on vertical structures. Journal of Waterway, Port, Coastal, and Ocean Engineering, Vol. 119, pp. 381-397.

Ramachandran, K., Genzalez, R., Oumeraci, H., Schimmels, S., Kudella, M., Van Doorslaer, K., De Rouck, J., Versluys, T., Trouw, K., 2012. Loading of vertical walls by overtopping bores using pressure and force sensors – a large scale model study. 33rd International conference on coastal engineering, Santander, Spain, p. 15.

Ramsden, J.D., 1996. Forces on a vertical wall due to long waves, bores and dry-bed surges, Journal of Waterway, Port, Coastal, and Ocean Engineering, Vol. 122, pp. 134-141.

Schmidt, R.; Oumeraci, H.; Partenscky, H.W., 1992. Impact loads induced by plunging breakers on vertical structrues. 23rd International conference on coastal engineering, Venice, Italy, p. 14. doi: https://doi.org/10.9753/icce.v23.%p

Streicher, M., Kortenhaus, A., Altomare, C., Gruwez, V., Hofland, B., Chen, X., Marinov, K., Scheres, B., Schüttrumpf H., Hirt, M., Cappietti, L., Esposito, A., Saponieri, A., Valentini, N., Tripepi, G., Pasquali, D., Di Risio, M., Aristodemo, F., Damiani, L., Willems., M., Vanneste D., Suzuki, T., Klein Breteler, M., Kaste, D., 2017. WALOWA (Wave Loads on Walls) – Large-scale experiments in the Delta Flume. Proceedings of the 8th SCACR conference 3rd – 6th October, Santander, Spain, p 11.

Streicher, M., Hofland, B., Lindenbergh, R. C., 2013. Laser ranging for monitoring water waves in the new Deltares Delta Flume. ISPRS Ann. Photogramm. Remote Sens. Spatial Inf. Sci., II-5/W2, 271-276, Antalya, Turkey, p 6. doi: 10.5194/isprsannals-II-5-W2-271-2013, 2013.

U.S. Army Corps of Engineers, 2002. Coastal Engineering Manual (CEM), Engineer Manual 1110-2-1100. *U.S.* Army Corps of Engineers, Washington, D.C. (6 volumes).

Van Doorslaer, K., Romano, A., De Rouck, J., Kortenhaus, A., 2017. Impacts on a storm wall caused by non-breaking waves overtopping a smooth dike slope. Coastal Engineering, Vol. 120, pp. 93-111. doi: 10.1016/j.coastaleng.2016.11.010.

Van Doorslaer, K., De Rouck, J., Van der Meer, J.W. and Trouw, K., 2012. Full scale wave impact tests on a vertical wall using the wave overtopping simulator, p. 6.

Veale, W., Suzuki, T., Verwaest, T., Trouw, K., Mertens, T., 2012. “Integrated design of coastal protection works for Wenduine Belgium”. 33rd International conference on coastal engineering, Santander, Spain, p. 10.

APPENDIX

[Table A1]

[Table A2]

LIST OF TABLES

Table 1. Qualitative comparison of Tsunami/Tidal/Dam break flow bore compared to short duration overtopping bore characteristics resulting from irregular and broken waves.

Type	Duration	Generation mechanism	Aeration	Interaction with other bores	Ratio bore crest length/building width
-	s	-	-	-	-
Tsunami/ Tidal/ Dam break bore	Long	Landslide, Earthquake, Tide, Dam break	Turbulent, aerated and foamy bore front/roller	No	Large (flow around structure)
Overtopping bore	Short (~ 0.5-3)	Wave breaking, Overtopping	Turbulent, aerated and foamy bore front/roller	Yes	Small (no flow around structure)

Table 2. Test parameter for selected tests representing design storm conditions for the Belgian coast with a 17000-year return interval +20% increase in wave height and period (Irr_1_F) and 1000-year return interval (Irr_4_F).

testID	Waves	h_o	h_t	A_c	$H_{m0,o}$	$H_{m0,t}$	$T_{m-1,0,o}$	$T_{m-1,0,t}$	$S_{m-1,0,t}$	β_o	$h_t/H_{m0,o}$
-	-	m	m	m	m	m	s	s	-	-	-
Irr_1_F	~1000	3.99	0.28	0.27	1.05	0.30	5.80	12.30	0.0014	0.2	0.27
Irr_4_F	~1000	3.79	0.08	0.47	0.87	0.22	5.41	12.05	0.0012	0.2	0.09

ANNEX

ANNEX 1. Details of the 30 highest impacts for test Irr_4_F of the WALOWA test program. Values are in model scale (Froude length scale factor = 4.3). The bore velocity and thickness are measured at Location 1 (Cappietti et al. 2018).

Impact Nr	**Impact type**	**Impact force**	**Bore pattern**	**Efficient overtopping**	**Max. thickness**	**Max. velocity**	**Max. run-up**
-	**-**	**kN/m**	**-**	**-**	**m**	**m/s**	**m**
1	quasi-static	1.01	regular	no	0.13	2.25	0.58
2	quasi-static	0.82	collision	no	0.17	1.97	0.53
3	dynamic	0.80	catch-up	yes	0.13	2.18	0.46
4	impulsive	0.70	plunging	no	0.05	1.66	0.30
5	dynamic	0.62	collision	yes	0.08	2.03	0.35
6	quasi-static	0.61	seq. overtopping	no	0.19	1.10	0.44
7	quasi-static	0.59	collision	no	0.08	2.23	0.45
8	quasi-static	0.58	collision	no	0.05	1.88	0.43
9	quasi-static	0.51	collision	no	0.18	0.51	0.44
10	impulsive	0.50	collision	no	0.03	1.70	0.20
11	quasi-static	0.49	collision	no	0.12	0.70	0.41

12	quasi-static	0.48	collision	no	0.07	1.74	0.41
13	quasi-static	0.48	regular	no	0.08	2.01	0.43
14	impulsive	0.48	collision	yes	0.09	1.01	0.28
15	quasi-static	0.44	regular	no	0.06	1.92	0.34
16	quasi-static	0.44	collision	no	0.10	1.41	0.35
17	quasi-static	0.44	regular	no	0.04	1.67	0.37
18	impulsive	0.41	catch-up	yes	0.04	1.48	0.30
19	quasi-static	0.40	regular	no	0.04	1.65	0.38
20	impulsive	0.40	seq. overtopping	yes	0.12	n.a	0.30
21	quasi-static	0.38	collision	no	0.06	2.11	0.33
22	impulsive	0.38	regular	no	0.04	1.71	0.31
23	quasi-static	0.36	collision	no	0.08	2.68	0.30
24	quasi-static	0.35	regular	no	0.06	1.66	0.32
25	quasi-static	0.35	collision	no	0.07	1.25	0.30
26	impulsive	0.32	seq. overtopping	no	0.08	1.33	0.24
27	dynamic	0.32	regular	no	0.06	1.46	0.27
28	quasi-static	0.31	collision	no	0.10	1.65	0.31
29	quasi-static	0.31	regular	no	0.05	1.65	0.33
30	quasi-static	0.30	collision	no	0.06	1.65	0.32

ANNEX 2. Details of the 30 highest impacts for test Irr_1_F of the WALOWA test program. Values are in model scale (Froude scale factor = 4.3). The bore velocity and thickness are measured at Location 1 (Cappietti et al. 2018).

Impact Nr	**Impact type**	**Impact force**	**Bore pattern**	**Efficient overtopping**	**Max. thickness**	**Max. velocity**	**Max. run-up**
-	**-**	**kN/m**	**-**	**-**	**m**	**m/s**	**m**
1	quasi-static	4.77	collision	no	0.30	3.43	1.22
2	impulsive	4.25	catch-up	yes	0.31	2.29	1.05
3	quasi-static	4.22	catch-up	yes	0.33	1.53	1.17
4	dynamic	4.20	plunging	yes	0.26	2.46	0.90
5	quasi-static	3.66	collision	no	0.31	1.79	1.10
6	dynamic	3.10	collision	yes	0.26	2.01	0.87
7	quasi-static	2.97	collision	no	0.26	2.68	0.98
8	quasi-static	2.22	collision	no	0.23	3.18	0.85
9	quasi-static	2.39	seq. overtop.	no	0.23	2.45	0.84
10	quasi-static	2.53	collision	yes	0.25	3.50	0.89
11	quasi-static	2.49	collision	no	0.23	1.80	0.84
12	dynamic	2.44	plunging	yes	0.24	3.21	0.70
13	quasi-static	2.26	catch-up	no	0.23	3.03	0.82
14	quasi-static	2.40	catch-up	yes	0.46	1.84	0.81
15	quasi-static	2.38	collision	no	0.30	1.25	0.90
16	quasi-static	2.29	collision	no	0.18	3.62	0.87
17	quasi-static	2.26	seq. overtop.	yes	0.20	2.65	0.81
18	dynamic	2.22	catch-up	yes	0.25	2.17	0.51
19	quasi-static	2.20	catch-up	yes	0.16	2.13	0.85
20	impulsive	2.15	seq. overtop.	no	0.21	1.51	0.49
21	quasi-static	2.13	seq. overtop.	no	0.21	2.66	0.84
22	quasi-static	2.12	collision	no	0.11	2.47	0.80
23	dynamic	2.10	plunging	yes	0.21	2.18	0.70
24	quasi-static	2.07	collision	no	0.20	3.35	0.86
25	quasi-static	2.06	collision	no	0.29	1.68	0.83
26	quasi-static	2.06	seq. overtop.	no	0.17	2.02	0.76
27	quasi-static	2.02	catch-up	yes	0.18	3.41	0.82
28	quasi-static	2.00	catch-up	no	0.27	2.62	0.82
29	dynamic	1.97	collision	yes	0.21	2.32	0.72
30	quasi-static	1.96	collision	no	0.22	3.54	0.78

841

842

843 **FIGURES**

844 Figure 1.

845

846 Figure 2.

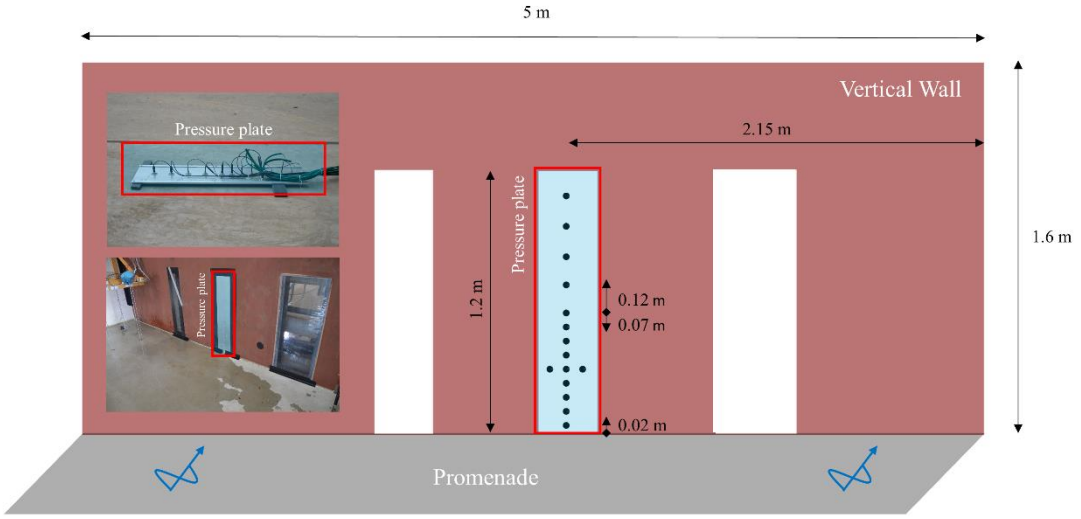

847

848 Figure 3.

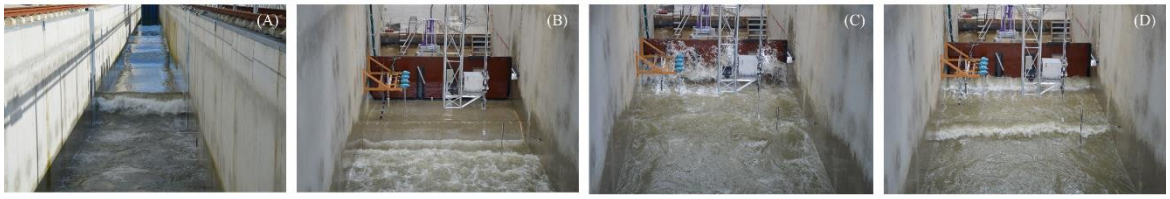

849

850 Figure 4.

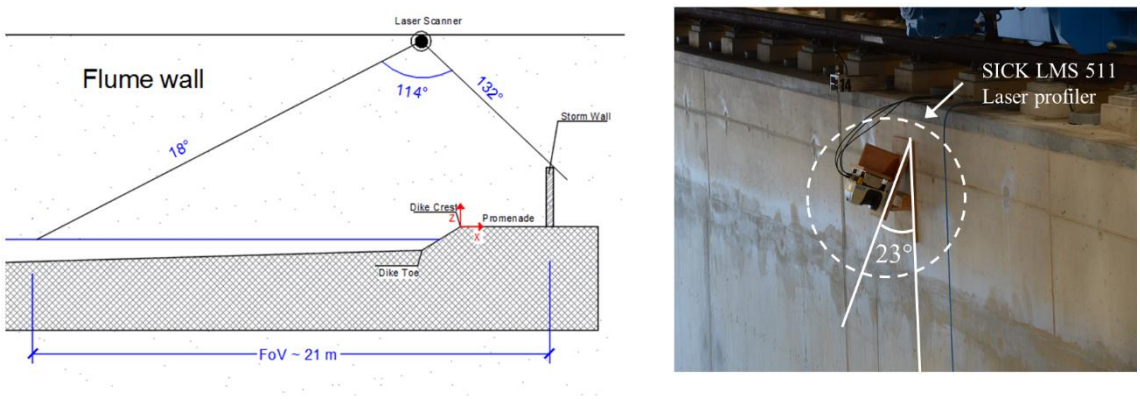

851

852 Figure 5.

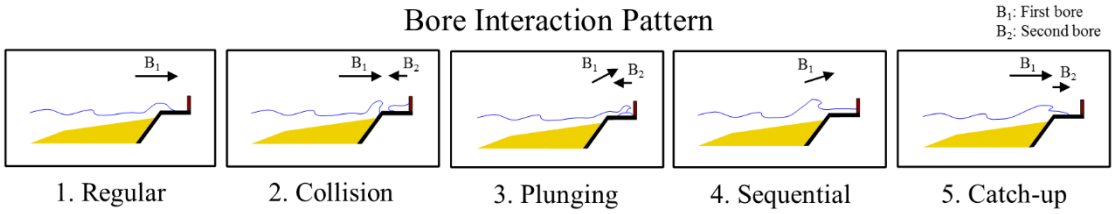

853

854 Figure 6.

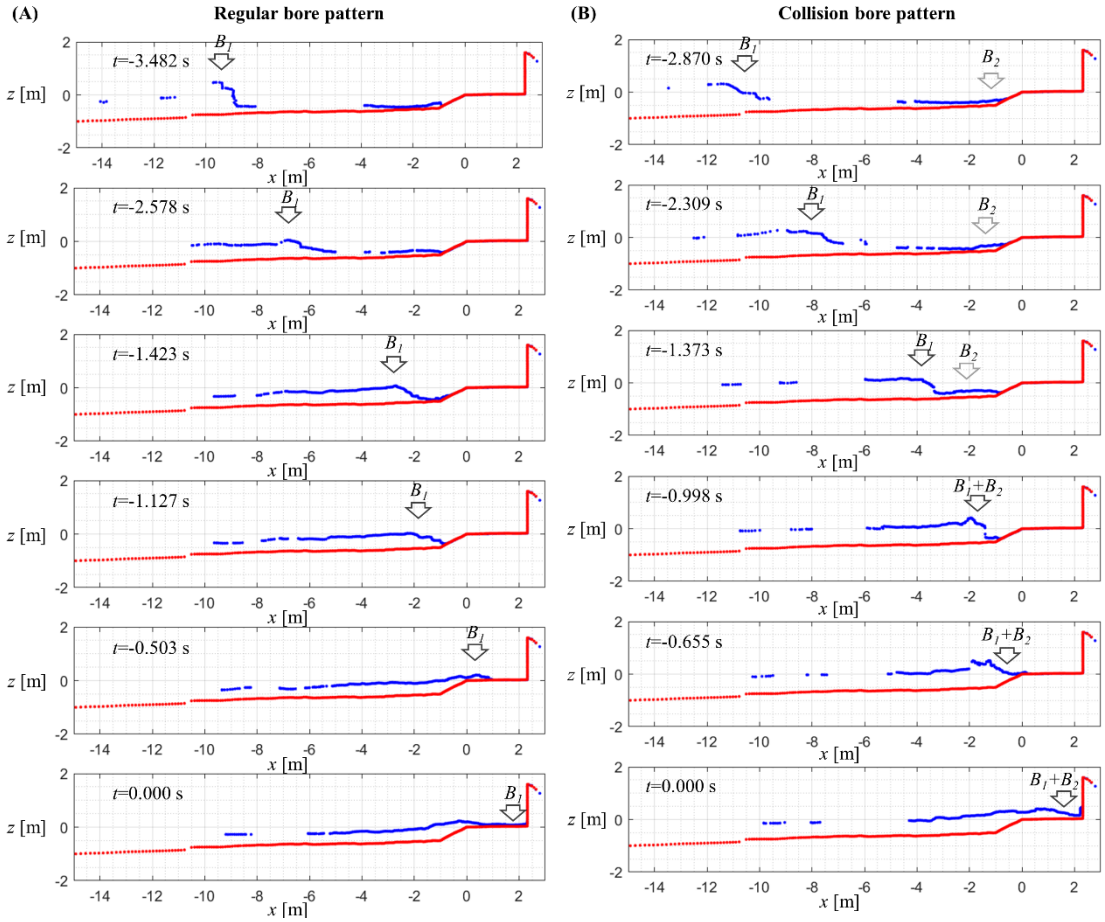

855

856

857

Figure 7.

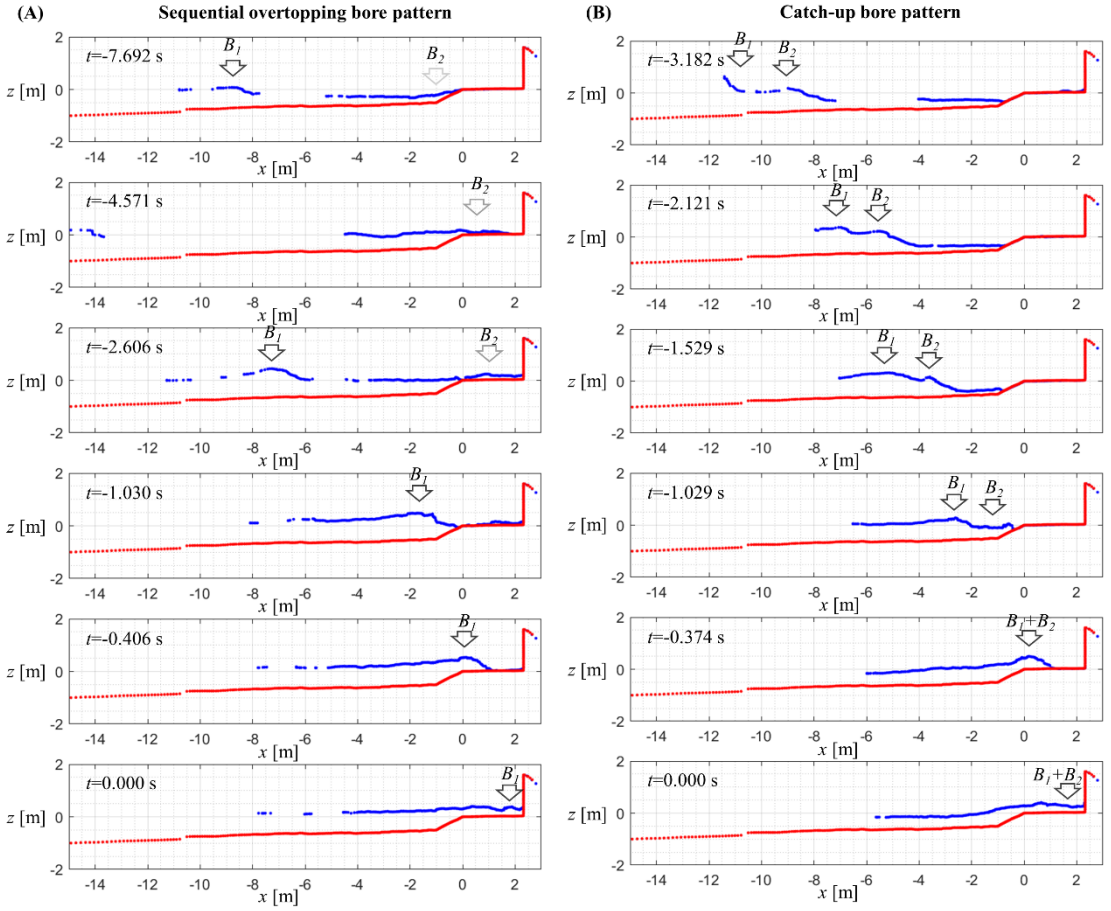

Figure 8.

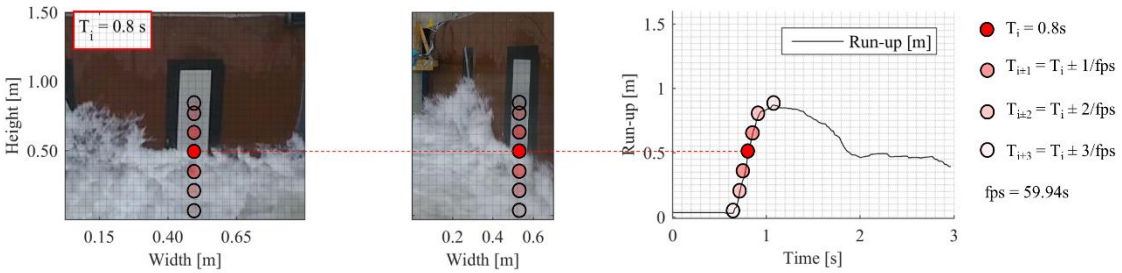

869

870

871

872

873

874

875

876 Figure 9.

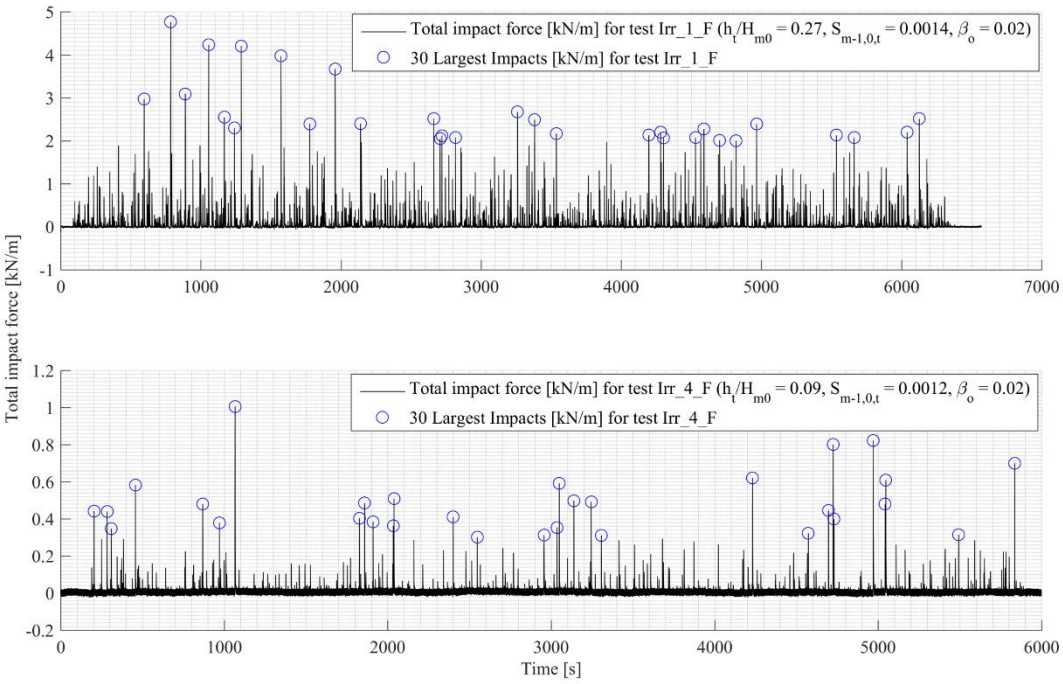

877

878 Figure 10.

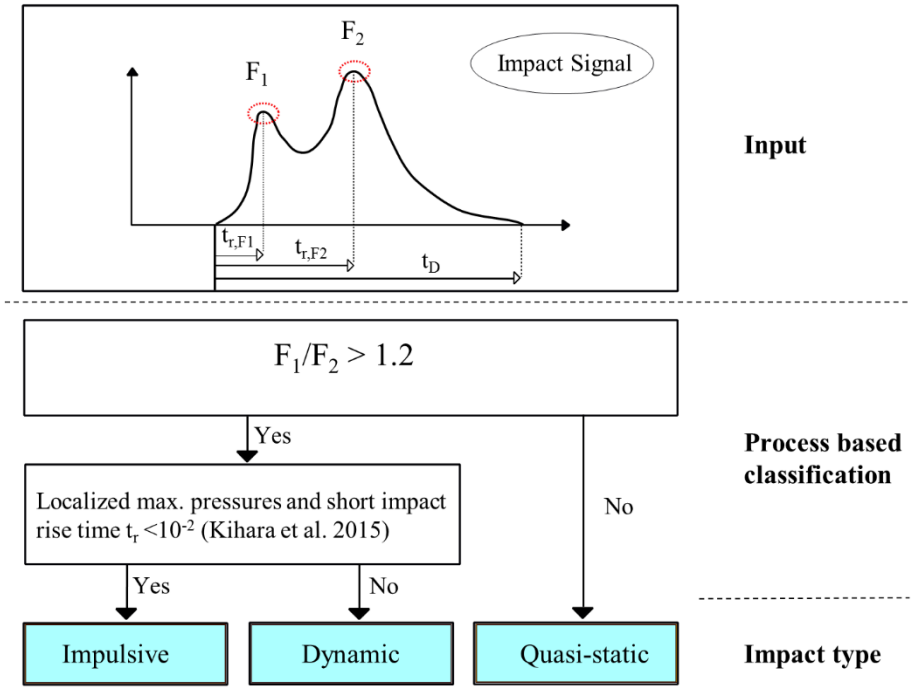

879

880 Figure 11.

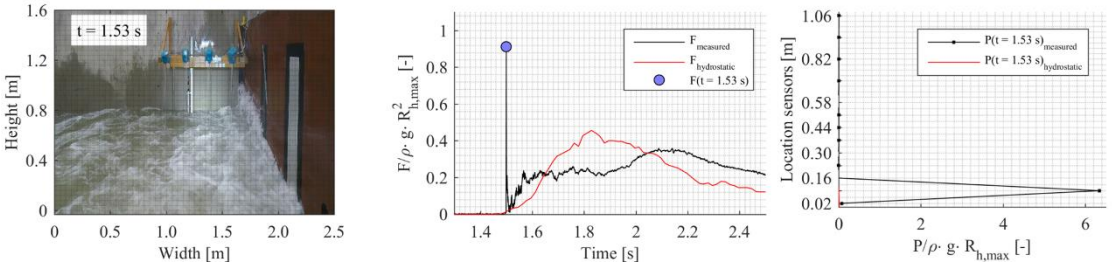

881

882 Figure 12.

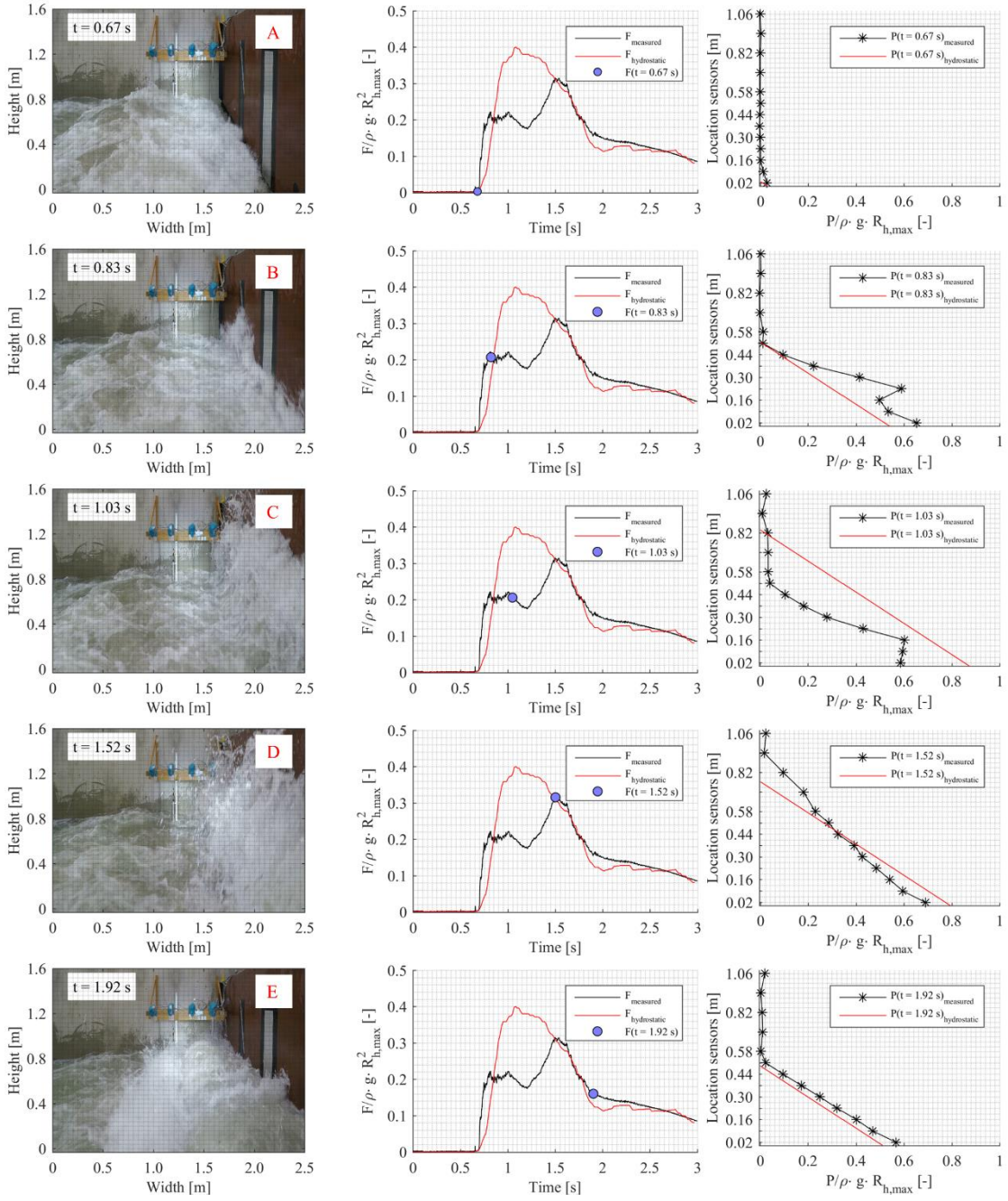

883

884

885 Figure 13.

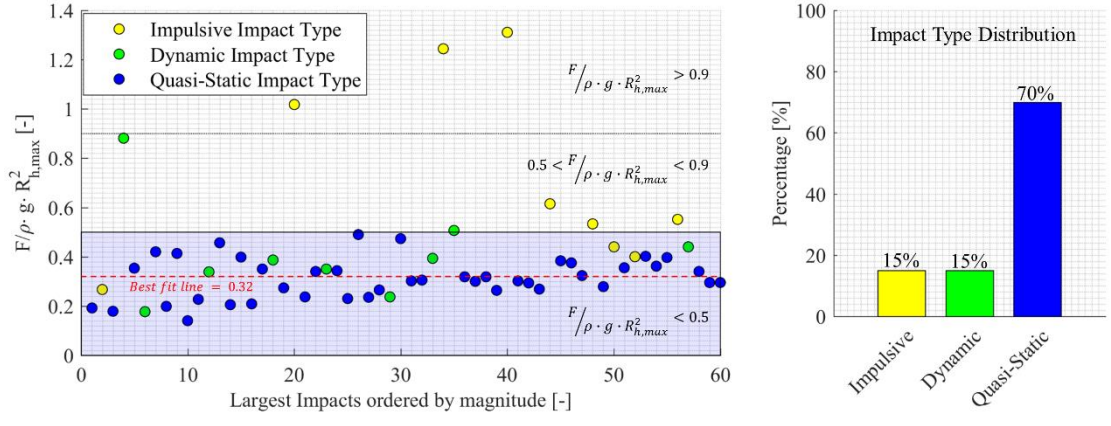

886

887 Figure 14.

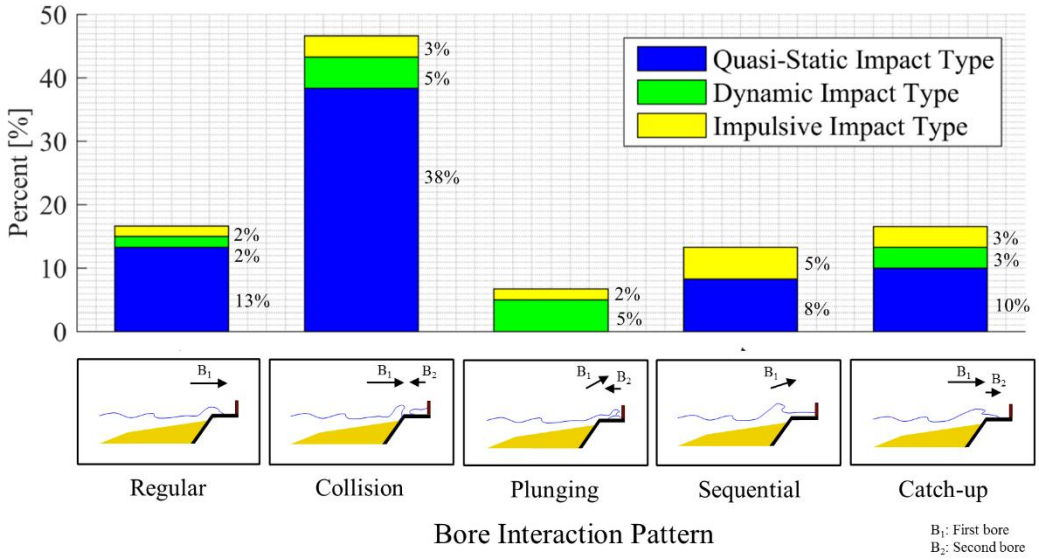

888

889 **LIST OF FIGURES**

890 Figure 1. Storm water level reaching the dike in Ostend, Belgium (A). The situation
891 before nourishments were carried out starting from 2007. Typical situation of the
892 Belgian coastline (B), comprised of a mild foreshore, dike, promenade and vertical wall
893 (picture by Nicolas Milot).

894

895 Figure 2. Overview drawing of the vertical wall installed in the Delta Flume to measure
896 the wave impacts. The pressure plate is highlighted within the red rectangular and the
897 location of pressure sensors on the pressure plate are indicated with black dots.

898

899 Figure 3. (A) An incoming wave breaking on the shallow and sandy foreshore. (B) 2
900 bore crests at the start of the overtopping process over the dike and (C) consecutive
901 impact of the bore against the vertical wall. (D) After the impact process the bores are
902 reflected and travel shoreward again.

903

904 Figure 4. The SICK LMS511 laser profiler was mounted to the left flume wall (when

905 standing with the back to the paddle) approximately at the dike toe location (A). A slant
906 angle of 23 degree was used to prevent dazzling of the device due to direct reflections in
907 nadir (B).
908
909 Figure 5. Sketch of the five identified bore interaction patterns (*1. regular, 2. collision, 3.*
910 *plunging, 4. sequential, 5. catch-up bore pattern*). The direction of travelling is indicated
911 with the black arrows for the first (B_1) and second (B_2) bore.
912
913 Figure 6. *Regular bore pattern* (A) observed before impact nr.1 from test Irr_4_F (see
914 ANNEX 1) and *collision bore pattern* (B) observed before impact nr.1 in test Irr_1_F (see
915 ANNEX 2).
916
917 Figure 7. *Sequential overtopping bore pattern* (A) observed before impact nr. 13 of test
918 Irr_1_F (see ANNEX 2) and *catch-up bore pattern* (B) observed for impact nr. 2 of test
919 Irr_1_F (see ANNEX 2).
920
921 Figure 8: Motion tracking method the bore leading edge in consecutive video images. The
922 video images where recorded by a top mounted (left) and side mounted (middle) GoPro
923 camera with 59.94fps and 0.002m spatial resolution. The situation at $T_i = 0.8$s is shown in
924 the two camera images and the resulting time series of instantaneous bore run-up at the
925 wall after the motion tracking was performed for impact nr. 7 of test Irr_1_F (see ANNEX
926 2) is displayed (right).
927
928 Figure 9. The time series of total impact force [kN/m] for test Irr_1_F (upper graph) and
929 test Irr_4_F (lower graph) and the 30 largest impacts for each tests highlighted with a blue
930 circle.
931

Figure 10. Impact type classification methodology

Figure 11. Impact nr. 20 of test Irr_1_F (see ANNEX 2) at the moment of impulsive impact (t = 1.53s). A sideview image of the situation (left), the dimensionless impact force (middle) and dimensionless impact pressures (right) are displayed.

Figure 12. Impact nr. 7 of test Irr_1_F (see ANNEX 2) in different stages of impact. A) Initial impact stage, B) deflection stage and dynamic impact type, C) moment of maximum run-up, D) reflection stage and quasi-static impact and E) hydrostatic stage are displayed. A sideview image of the situation (left), the dimensionless impact force (middle) and dimensionless impact pressures (right) are given for each impact stage A-E.

Figure 13. Distribution of impact types for the 60 largest impacts of test Irr_1_F and test Irr_4_F (30 from each test). The percentage distribution (right graph) and the distribution in dependence of the non dimensionless impact force (left graph) is shown.

Figure 14. Link between the five bore interaction patterns (1. *Collision bore pattern* of an incoming and reflected bore colliding, 2. *Catch-up bore pattern* with a second bore overtaking a first bore, 3. *Regular bore pattern* with no significant interactions observed, 4. *Sequential overtopping bore pattern* of an incoming bore sliding over a residual water layer from previous impacts 5. *Plunging bore pattern* with breaking of the incoming bore over a reflected bore against the wall) and the three impact types (1. *Impulsive impact type*, 2. *Dynamic impact type* and 3. *Quasi-static impact type*).